CHAPTER 3

EXPERIMENTAL PROCEDURE

3. Experimental section

This chapter includes a comprehensive explanation for the synthesis of substituted Y-type barium hexaferrite (Co_2-Y), utilized in overall research work, along with characterization techniques and application processes. All the chemicals are from Merck, India (GR grade with 99.9% purity).

3.1 Y-type barium hexaferrite synthesis through the sol-gel auto combustion process

The synthesis of the hexagonal ferrite is considered enormously intricate due to the possible overlapping of different hexagonal phases (excepting M-type hexaferrite) within a narrow temperature range. In continuation to achieve a single Y-type barium hexaferrite, the calcination temperature needs to be exceeded from 1000^{o}C resulting in the particle size enlargement with a broad particle size distribution. In consideration of the problem associated with discontinuous grain growth (DGG), a suitable material synthesis route need to be selected [(Pullar 2012)]. There are multiple possible routes to prepare single-phase Y-type barium hexaferrite, such as the solid-state ceramic route, coprecipitation method, molten-salt method, sol-gel method, hydrothermal method, microemulsion method [(Chandel *et al*. 2020)]. To achieve a chemically homogenized and fine-grained polycrystalline hexaferrite, a nitrate-based sol-gel auto combustion process is adopted.

The nitrate-citrate sol-gel auto combustion method, also known as gel-thermal decomposition or low-temperature self-combustion method, or low-temperature auto-ignition method, has been employed to prepare chemically homogenized substituted Y-type barium hexaferrite (Co_2-Y). This method involved several advantages over the other processes in terms of inexpensiveness & simple experimentation [(Yue *et al.* 1999)]. This process consists of a self-nourishing & thermally-encouraged anionic redox reaction (exothermic in nature) of xerogel, which is attained from drying of an aqueous solution

comprising anticipated metal nitrates (acts as an oxidizer) and organic complexant or chelating agent (act as a reductant) [(Airimioaei *et al.* 2011)]. Raw materials like barium nitrate [$Ba(NO_3)_2$], cobalt nitrate [$Co(NO_3)_3.6H_2O$], iron nitrate [$Fe(NO_3)_3.9H_2O$], and citric acid [$C_6H_8O_7.H_2O$] have been used in the auto combustion process. In all nitrate salts, quantitative metal ion content in the solution is maintained through chemical analysis. The solutions are prepared, and the molarities of the solutions are determined. 1M metal nitrate solution of each nitrate salt is prepared and kept separately. Before synthesis, chemical analyses of the solutions are carried out to see the actual metal ion concentration.

The stoichiometric moles for each metal nitrate precursor and fuel are calculated (1:1 for metal nitrates and fuel), weighted and mixed within deionized water with the help of a magnetic stirrer. The selection of metal nitrates as a precursor favors the combustion process by delivering NO^{-3}, an excellent oxidant source [(Selvan *et al.* 2003)]. The method also offers various fuel agents (complexant) choices, such as urea, glycine, and citric acid. The selection of citric acid (decomposition temperature of 175°C, combustion heat of –2.76 kcal/g)) as a complexant or fuel favors the moderate rate of combustion, avoiding secondary phases & a higher temperature value of around 500°C during combustion [(Sutka and Mezinskis 2012), (Costa *et al.* 2010)]. Fig. 3.1 shows the synthesis method of barium hexaferrite (Co_2-Y).

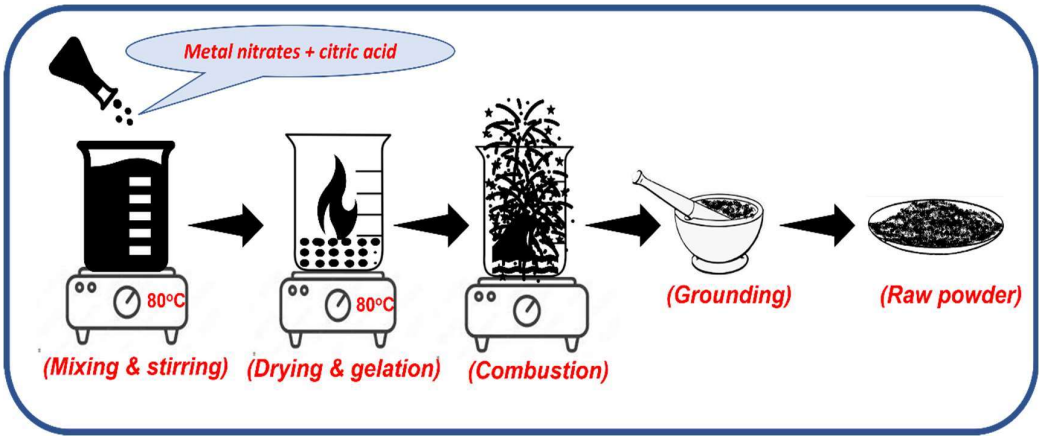

Figure 3.1 Schematic diagram of the nitrate-based sol-gel auto combustion process.

The pH level of this solution is tuned at seven by dropwise addition of ammonium hydroxide (NH_4OH) solution. The tuning of the pH value also favors the process as it enhances the metal ion chelating and controls oxygen balance, enhances the crystallinity of ferrite, and helps the formation of three-dimensional porous nitrate-citrate-based xerogel (especially while using citric acid as a fuel) [(Junliang *et al.* 2009)]. The selection of pH level 7 can be justified due to the incomplete complexion of Fe^{3+} ions, less oxygen balance, and diminished crystallinity below pH of 6 or 7, whereas the pH level beyond 7 causes a high combustion rate & temperature resulting in the abnormal particle growth [(Yue *et al.* 2004)]. The admixture is allowed to be heated at 80°C for slow evaporation of the solvent, which favors the 3D networking of the chelating agent with metal ions. The prolonged evaporation causes the formation of porous gel and ignition of this gel, resulting in fluffy burnt ash. The burnt ash is ground using a mortar pestle to obtain the fine powder. The raw powder is calcined at 1200 °C for 2 hrs to enhance the degree of crystallization and allows the needful allocation of cations to their specific site in the hexagonal ferrite. The calcination temperature is fixed at 1200°C due to the formation of impurity phases (M-type hexaferrite and other spinel ferrite phases) at low temperature and the gradual disappearance of the Y-type hexaferrite phase above it (forming other complex hexagonal ferrites) [(Alrebdi *et al.*, 2022)]. The as-obtained calcined powder is ground using a mortar pestle. Then, the powder is granulated using three wt% of polyvinyl alcohol (PVA) solution as a binder and pressed into a disc-shaped (10 mm diameter) pellet (for further characterization) by applying 6 tonnes per cm^2 pressure (~ 600 MPa) using a hydraulic press. These pellets are sintered at 1050°C for 2 hrs with a heating rate of 3°C/min in the controlled muffle furnace (OKAY Furnace, Bysakh and Co., India). After that, cooling is applied to the sample with a 3°C/min rate up to room temperature.

3.2 Characterization of hexaferrite samples

After the synthesis of substituted hexaferrite samples, the calcined powders are studied using the following techniques;

3.2.1 X-ray diffraction analysis

The X-ray diffraction (XRD) technique is an essential, non-contacting, non-destructive method to identify the crystalline phases and other structural parameters. The XRD pattern can be utilized to determine atomic structures in both a qualitative and quantitative manner. As most of the physical properties of the materials are sensitive to the structural specifications (atomic positions, crystallite size, shape, orientation, etc.), it becomes crucial to investigate the material using the XRD pattern.

In the case of crystalline structures, the atomic arrays are organized in an even and recurring pattern. The unit cell is the smallest repeating element, which creates a three-dimensional stacking order. In three-dimensional order, the shape and size of the unit cell can be explained using three axes (a, b, c) and the angles between them [(Stanjek and Häusler 2004)]. A lattice is a periodic arrangement of points collection in a crystal that can be denoted by a set of translation vectors in both two and three-dimensional arrays. The *(hkl)* values are termed as the Miller indices for a plane or a face which can be determined by making a perfect integer value to the reciprocals of the intersections corresponding to the x, y, and z-axis in a particular lattice plane [(Stanjek and Häusler 2004)].

The interaction of electromagnetic waves with atomic structures of any material provides a diffraction effect only if the wavelength of the incident wave and the periodicity of the crystals are comparable in magnitude. Electromagnetic waves having wavelengths in order of 10^{-10} m are termed X-rays, which are comparable with the lattice parameters for most of the crystals. The X-rays can be generated by bombarding a target (having a high

atomic number) using electromagnetic radiation (having sufficient energy), which results in releasing an electron from the *K*-shell. This *K*- shell electron is filled by other electrons coming from the outer shells (from *L* or *M* shells); the energy difference during this migration of electrons is emitted in the form of X-rays.

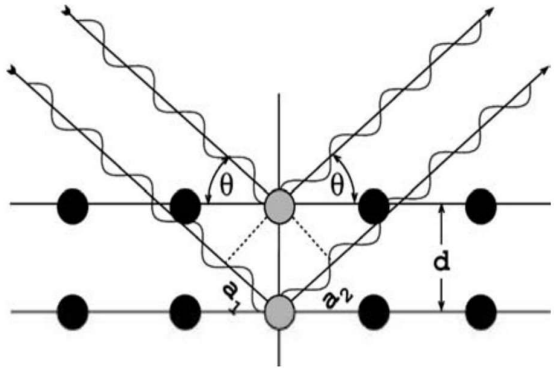

Figure 3.2 Schematic representation of regularly spaced atomic planes and their interaction with incident X-ray radiations [(Stanjek and Häusler 2004)].

According to the Bragg's law, if an X-ray interacts with the atomic planes (shown in Fig. 3.2), the interference is constructive (so-called Bragg reflection) only if the path difference between the incident and scattered ray ($a_1 + a_2$, in Fig. 3.2) is a perfect integer multiple of the wavelength. The condition to achieve constructive interference, the Bragg law, must follow the following equation

$$n\lambda = 2\, d\, Sin\, \theta \qquad (3.1)$$

Where λ shows the incident wavelength, θ indicates Bragg's angle measured with respect to the crystal planes, *d* shows inter-planer spacing, and n is the diffraction order. In the present work, the phase identification is performed using the X-ray diffraction pattern obtained using Rigaku Miniflex 600 benchtop diffractometer with Cu-Kα (1.5406 Å) radiation. The instrument is operated at 45 kV and 200 mA with Cu as a target material. The data is recorded with a step size of 0.02 (degree) step size and a count time of 4 s for

each step. The phase identification has been performed by Philips X-pert high score plus software, which works with the Hanawalt method. The Hanawalt search method has been developed at the ICDD, which involves sorting the XRD patterns according to their *d*-spacing value corresponding to the highest intensity peak. The as-obtained XRD pattern is evaluated by the set of peak positions (2θ) and respective relative intensities (*I*). The angular positions of peaks (2θ) depend on the incident radiation wavelength and interplanar spacing *(d)* of lattice planes. By matching these two factors, the presence of phase is confirmed, and other structural parameters are obtained using the following relations;

$$D_m = \frac{k_s.\lambda}{W_{hkl}.Cos\theta} \tag{3.2}$$

Where D_m is the mean crystallite size, k_s represent the Sherrer's constant, λ is the X-ray wavelength (λ = 1.54056 Å), W_{hkl} is the FWHM value for the particular peak, and θ is the corresponding Bragg's angle. For precise calculation of crystallite size, the instrumental line broadening component can be subtracted from the measured FWHM value to achieve the actual line broadening (FWHM) value, using the following relation:

$$W_{hkl}^{actual} = \sqrt{\left(W_{hk}^{measured}\right)^2 - \left(W_{hkl}^{instrumental}\right)^2} \tag{3.3}$$

In this work, the standard silicon (Si) sample is utilized for the correction of instrumental broadening, having W_{hkl} around 0.09821, at a peak position of 29° (2θ) with (111) (*hkl*). The structural parameters are obtained by using the following relations given below;

$$\frac{1}{d^2} = \frac{1.34\,(h^2+hk+k^2)}{a^2} + \left(\frac{l}{c}\right)^2 \tag{3.4}$$

$$V_{uc} = 0.8660\,.c.a^2 \tag{3.5}$$

$$D_x = \frac{M_w.Z_e}{N_a V_{uc}} \tag{3.6}$$

$$W_{hk}\,.Cos\theta = \varepsilon.(4.Sin\theta) + (\lambda k_s/D_m) \quad (3.7)$$

Where d represents the inter-planer spacing, h k and l are miller indices for a particular plane, a and c are the major and minor axis of a hexagonal lattice, V_{uc} is unit cell volume, D_x is X-ray density, M_w is for molecular weight, Z_e is the effective number of formula units within a single unit cell (Z_e = 3 for Co_2-Y), N_a is Avogadro's constant, i.e., 6.023×10^{23}, and ε is lattice strain.

3.2.2 Fourier–transform infrared spectroscopy

FT-IR, meant for Fourier Transform InfraRed, is considered an ideal infrared spectroscopy method. While passing an IR radiation through a sample, a portion of this incident infrared radiation is absorbed by the sample itself, and a fraction of it transmits through the sample. The detection of this outcoming spectrum represents the specific molecular absorption along with transmission and provides a molecular fingerprint of the sample. The individual absorption peak represents the unique vibrational frequency of a specific atomic bond present in the material. Therefore, infrared spectroscopy can be considered a prominent technique in positive identification (qualitative analysis).

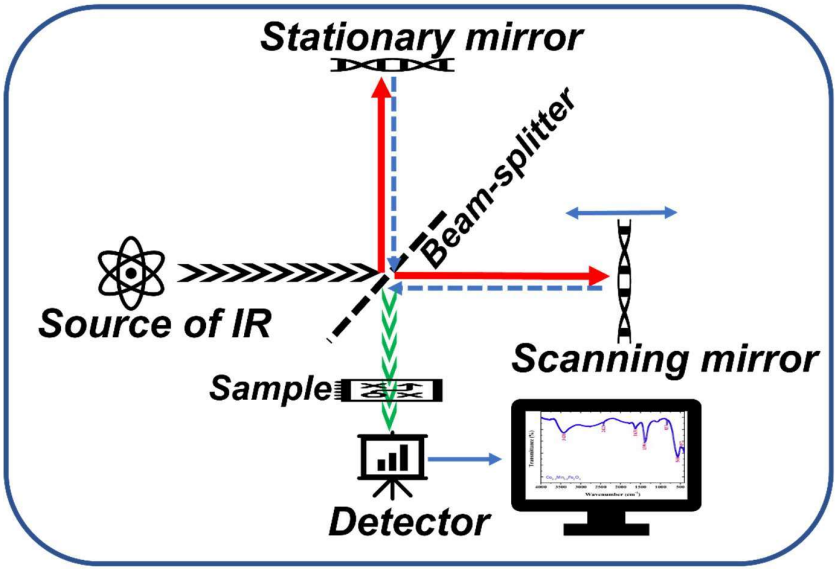

Figure 3.3 Schematic representation of working principle for FTIR spectrometer.

Fig. 3.3 shows the schematic representation of the working principle for the FTIR spectrometer. The FTIR instrument uses a beam splitter to divide the infrared beam coming from the IR source in two different directions. One reflects off from a flat mirror (fixed) and another from a moving mirror (characteristically a few millimeters only). The two beams recombine at the beamsplitter and interfere with each other due to a continuous path difference. This signal is called an interferogram, having exclusive data point information coming from the IR source. A mathematical algorithm is used to generate the output data for FTIR in terms of absorption at each wavelength, i.e., Fourier transformation. It converts the interferogram signal from the mirror positioning to the wavenumber (cm^{-1}) after transmitting from the sample.

The FTIR measurements are executed in transmittance mode (ATR mode) from 400 to 4000 cm^{-1} at room temperature with Nicolet iS 5 FTIR Spectrometer by Thermo Scientific, with an excellent spectral resolution of 0.5 cm^{-1}. The FTIR data are plotted using origin pro software and determined for the peak positioning of the absorption peaks for further investigation of bond length (Fe-O) using its relationship with force constant, as explained with the following equations:

$$L_b = \sqrt[3]{\left(17/F\right)} \tag{3.8}$$

$$F = (2\pi \upsilon_{wn} c_{vl})^2 . \mu_{em} = (2\pi \upsilon_{wn} c_{vl})^2 . \left[\left(M_1 x\, M_2\right)/\left(M_1 + M_2\right)\right] \tag{3.9}$$

Where L_b represents the bond length, F is for force constant, υ_{wn} is the wavenumber corresponding to the specific absorption band, c_{vl} is the speed of light, μ_{em} is the effective mass of bonded atoms, M_1 and M_2 are the atomic weights of bonded atoms.

3.2.3 Surface area analysis using BET

The BET theory (developed by Stephen Brunauer, Paul Emmett, & Edward Teller) is an extended version of the Langmuir theory (proposed by Irving Langmuir) in 1916. This theory correlates the monolayer adsorption of gaseous molecules over the surface (θ_{fs}) with gas pressure (P_g) according to the following relationship [(Raja, P. M. V., & Barron 2021)].

$$\theta_{fs} = \frac{\alpha_c}{(1+P_g.\alpha_c)} \tag{3.10}$$

Where α_c is a constant. The validity of the Langmuir theory is limited by several assumptions, such as the adsorption energy of all sites should remain the same, adsorption needs to be independent of the adsorption at an adjacent site, and the adsorption capability needs to be dependent on the concentration of adsorbate, it needs to prepare a monolayer only, each active site requires to adsorb only single molecule of the adsorbate. These flaws within the Langmuir theory can be improved considering the BET theory, where the adsorbed gas amount is not considered as a function of active or exposed surface only; it also depends on the gas pressure, temperature & interaction between the gas and solid.

The utilization of nitrogen as an adsorbate is favored due to the easy availability and intense interaction with most solid materials. The material is cooled using liquid nitrogen gas to facilitate the adsorption of the solid. A precisely measured amount of nitrogen gas is released and adsorbed over the surface of the material's surface under a partial vacuum condition. The pressure-dependent adsorption reaches its saturation, and no more adsorption of molecules is allowed to form secondary adsorption. The pressure variation during all this adsorption process is measured using highly sensitive transducers. After that, the sample chamber is removed from the nitrogen contact and heated to release the adsorbed nitrogen molecules. The releasing amount of this nitrogen is quantified in terms of gas volume. The instrument provides the plots between the amount of adsorbed nitrogen gas and variation within the relative pressure. There are five types of adsorption

isotherms possible. These isotherms are categorized in five different categories, depending on the relative pressure and BET constant values. By analyzing these isotherms, the surface area of the ferrite sample can be determined using the BET equation [(Raja, P. M. V., & Barron 2021)]:

$$\frac{1}{X\left[\left({}^{P_0}/_{P}\right)-1\right]} = \frac{1}{C.X_m} + \frac{(C-1)}{C.X_m}\left({}^{P_0}/_{P}\right)^{-1} \quad (3.11)$$

Where X is the measured weight of nitrogen adsorbed at a relative pressure of (P/P_o), C is constant, X_m is the volume required to achieve single layer adsorption of gas at standard temperature and pressure (STP, i.e., 1 atm pressure and 273 K temperature). To determine the sample's surface area using BET measurement, at least three data points need to lie within the relative pressure (P/P_0) range of 0.025 to 0.30. Once the gas volume (X_m) is achieved using the BET equation, the sample surface area (S_a) can be determined using the following equation [(Raja, P. M. V., & Barron 2021)]:

$$S_a = \left(\frac{N_a A_m}{M_v}\right).X_m \quad (3.12)$$

Where N_a is the Avogadro number (defined as the number of units per mole, having a numerical value of 6.022×10^{23}), A_m represents the cross-sectional area (for nitrogen gas, it is 0.162 nm^2), and M_v is the molar volume (*volume* occupied by one mole of gas) of adsorbate and equals 22.414 L at STP condition. In this research work, the ferrite samples have been analyzed using Quanta-chrome Autosorb (Model No: Nova 1200 BET) for the determination of surface area, total pore volume (At P/P_0= 0.990), and Mean pore diameter (nm) to explain the surface dependent behavior of the sample.

3.2.4 Nuclear magnetic resonance spectroscopy

Nuclear magnetic resonance (NMR) spectroscopy is an enormously valuable technique for both the identification and analysis of important organic compounds. As the

nuclei of an atom act like a tiny magnet, it allows the alignment toward the polarity of the externally applied magnetic field. The NMR spectroscopy quantifies the energy required to align the nuclei along the field. It can be clarified that considering a single proton (^{1}H) within the presence of an external magnetic field; there may have two possibilities, either parallel to the field (low energy state or stable state) direction or in the opposite direction (high energy state or unstable state). In terms of energy balance, both these situations are not similar; extra energy is required to maintain the unstable state of nuclei spin.

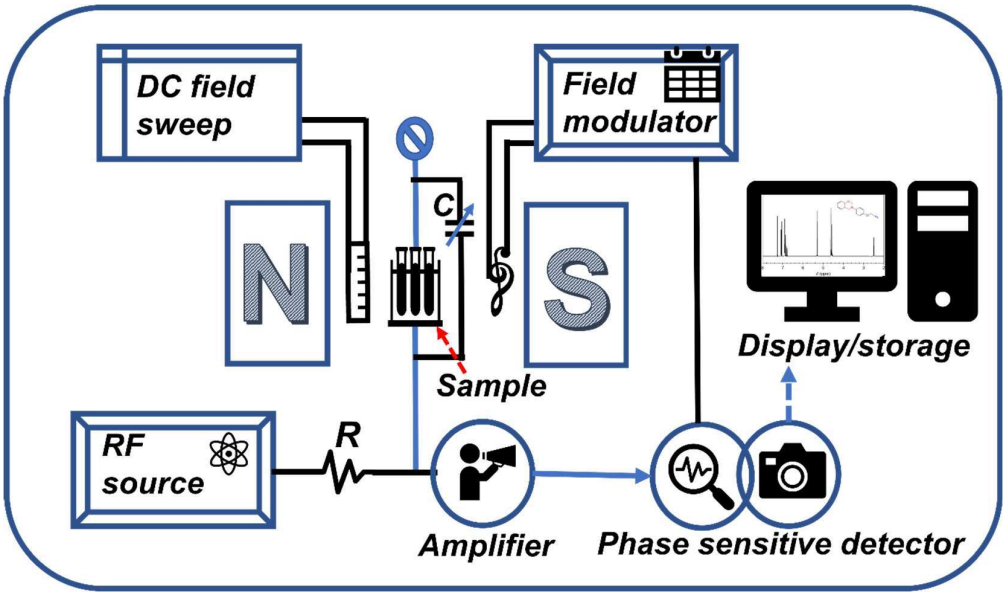

Figure 3.4 Schematic representation of working principle for NMR spectrometer.

Fig. 3.4 shows the schematic representation of the working principle for the NMR spectrometer. Whenever any organic compound is placed between the transmitter coil and the magnetic field strength increases steadily, a certain amount of energy (radio frequency energy) absorption takes place at a particular magnetic field value. In the case of ^{13}C NMR earlier, it is harder to detect the magnetic resonance due to less magnetic moment (5700 times less) in comparison to the single proton NMR. It is important to notice that ^{13}C shifts in ppm scale are much greater than ^{1}H protons due to the utilization of *p* orbitals by carbon

in bond formation. In contrast, hydrogen uses *s* orbitals [(Roberts and Caserio 1977)]. The NMR spectra provide the atomic composition within a molecule using chemical shifting, neighboring atoms or surroundings using spin-spin coupling constant, informs about the molecular dynamics by measuring relaxation time, and quantitative information regarding compounds using the signal intensity data. In the present work, all the organic compounds have been characterized using both ^{1}H and $^{13}C\{^{1}H\}$ NMR spectra to confirm their chemical identities, recorded using a JEOL ECS-400 spectrometer (operating at 400 MHz for ^{1}H and 100 MHz for ^{13}C).

3.2.5 Scanning electron microscopy (SEM) with EDS analyzer

Scanning electron microscopy, or SEM, generates a comprehensive and high-resolution magnified view of any object by scanning its surface using a focused electron beam. As shown in Fig. 3.5, the basic component of the instrument consists of an electron gun, producing an electron beam, which is confined up to a narrow size of approximately 0.4-5 nm in diameter by using condenser lenses [(Whan 2018)].

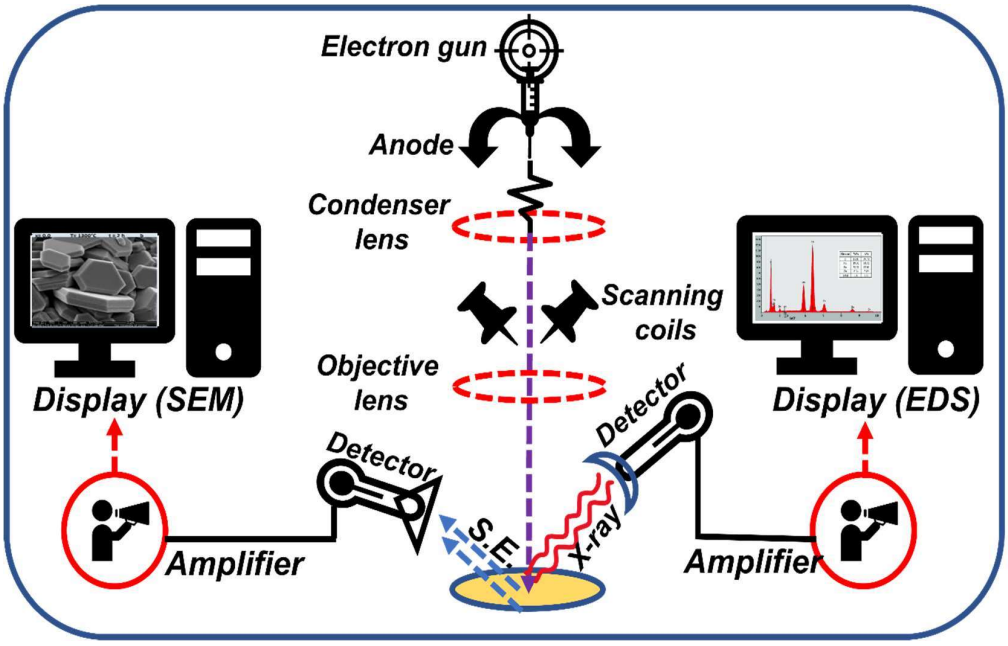

Figure 3.5 Schematic representation of working principle for SEM and EDS analyzer.

The beam then passes through a pair of scanning coils to deflect the beam before interacting (raster scanning) with the sample's surface. The electron beam loses its energy in terms of scattering and absorption. The electron beam's interaction is responsible for generating various signals, including secondary electrons (SE), back-scattered electrons (BSE), and representative X-rays. Each of these signals has been detected using different detectors adjusted with the instrument. Generally, secondary electrons (obtained by inelastic scattering) are utilized to generate SEM images. The phase contrast within the sample can be enhanced by collecting back scattered electrons (sensitive to the atomic number), which results from the elastic scattering interactions with electrons within the sample. The representative X-rays are also generated by releasing an electron from the inner shell; as the electron comes from the outer shell (having high energy) to fill that vacancy, the energy difference is released in the form of X-rays. The précised measurement of these X-ray signal wavelengths may help to confirm the elemental composition and their distribution [(Whan 2018)].

In the present research work, the surface morphology of powder particles and sintered specimen are studied using EVO - scanning electron microscope MA15/18 (developed by CARL ZEISS MICROSCOPY LTD.). The elemental analysis has been carried out using energy-dispersive X-ray spectroscopy (abbreviated as EDX, EDS, or XEDS) detector (model no. 51N1000 – EDS System, developed by Oxford Instruments Nanoanalysis) attached to the same SEM unit. The particle size or grain size measurements are carried out using ImageJ software (a free-ware image processing platform formerly developed by the National Institutes of Health, U.S.) software with a scaled line method [(Rishi and Rana 2015)].

3.2.6 Magnetic property measurement system (MPMS) analysis

The term “Magnetometry” meant for the measurement of sample magnetization in terms of the magnetic moment. Generally, a SQUID system can be explained as a black box that provides an extreme level of gain during the current or flux to the voltage amplifier. Over the last few years, the development of ultrathin films, nanoparticles, and dilute magnetic semiconductors (samples having a low moment) requires the measurement of magnetic properties equipped with high sensitivity [(Buchner *et al.* 2018)].

Magnetic measurement is measured using a vibrating sample magnetometer equipped with a superconducting quantum interference device (SQUID) with a highly sensitive fluxmeter, which can measure the sample's magnetization within varying temperatures (2 K – 1000 K) and a magnetic field of 7 Tesla. The measured quantity of calcined ferrite powder is filled within a Teflon capsule to study the hysteresis loop behavior and thermomagnetic properties in standard mode (2 K – 400 K of range) with a brass holder. To analyze the thermomagnetic properties at a higher temperature (oven module), the sintered pellet of the preferred dimension (2 mm x 2 mm x 4 mm) is analyzed with a heater stick.

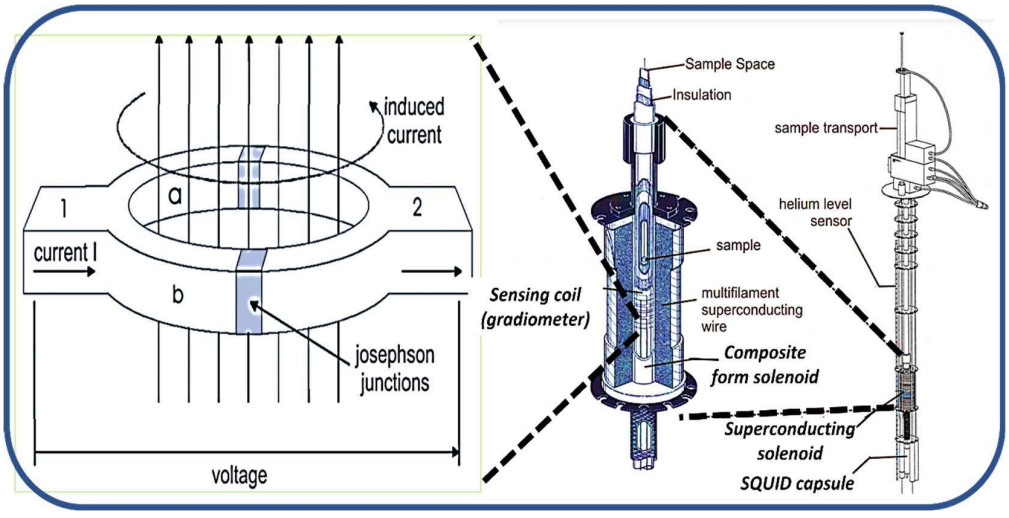

Figure 3.6 Schematic sample assembly representation and a magnified view of VSM head and SQUID junction [(Barth 2007)].

A schematic diagram of the sample handling system along with a magnified view of the magnetization detection system using SQUID-based coils are displayed in Fig. 3.6. The key factor behind achieving such a remarkable sensitivity comes with the Superconducting Quantum Interference Device (SQUID) sensor made of two parallel Josephson Junctions. The junction includes two superconductors, separated by each other using a thin insulating layer as shown in the left-most portion of Fig. 3.6 [(Barth 2007)].

The working principle of SQUID was first proposed by B. D. Josephson (1962), which states that a current is built (known as supercurrent) with an extremely critical value (I_C) and flows uninterruptedly through the weak link deprived of any voltage across the Josephson junction via tunneling of Cooper pairs. Since the SQUID sensor has a superconducting ring, thus it permits only a certain value of magnetic flux through it, whose magnitude is the integral multiple $\Phi_0 = 2.07 \times 10^{-15}$ Tesla-m^2 (flux quantization in superconductor). While maintaining the flux quantization, a screening current is induced in this superconducting ring corresponding to any variation within the magnetic flux. The minor magnitude of Φ_0 (integral multiple) allows advancing an enormously sensitive magnetic sensor, i.e., SQUID. Due to the flux quantization sensitivity in superconductors, the magnetic flux related to any materials can be converted to voltage using SQUID. The external biased current through the SQUID prompts the electron cooper pairs to tunnel via the weak link junctions. Whenever an external magnetic field is developed by the materials reaching the SQUID ring, it changes the critical current value within the superconductor. This alteration in current value is amplified as a voltage signal using electronic instrumentation calibrated to provide the magnetic moment. Hereafter, the SQUID can be understood as a highly sensitive flux-to-voltage transducer that can transform an enormously slight change of magnetic flux into a voltage signal [(Buchner *et al.* 2018)].

The MPMS3 system offers three different modes of magnetization measurements, including AC susceptibility mode, DC scan mode, and VSM (vibrating sample mode). The VSM mode (dependent on Faraday's electromagnetic induction law) is utilized to investigate the hysteresis behavior within all ferrite samples. According to this law, alternating electricity within any circuit causes a magnetic field and vice versa. In VSM mode, the sample is exposed to a uniform external magnetic field. The sample gets magnetized due to aligning the magnetic dipole, and the net magnetic moment increases with increasing field strength. The magnetic moment induces a supplementary field (known as a stray field) nearby to the sample and changes with the vibration of the sample. The alteration of this minor field is sensed by a set of exceedingly sensitive SQUID-based pick-up coils. This changing magnetic field provides an electric field (According to Faraday's law) and consequently an induced current relative to the material's magnetization. Finally, the signal is converted to the corresponding magnetic moment of the sample under investigation using the computer, which is calibrated with some standard samples.

A closer investigation of the magnetic hysteresis loop (obtained by MPMS3) shows that the magnetization of these ferrite samples (investigated within this research work) doesn't get saturated within the maximum applied field. The law of approach (proposed by Stoner–Wohlfarth) is employed to estimate the actual value of saturation magnetization (M_s). According to this proposal, magnetization can be explained in the following relation [(Fattouh *et al.* 2021)];

$$M = M_s \left[1 - {}^{A}/_{H} - {}^{B}/_{H^2}\right] + H.\chi \qquad (3.13)$$

Where M_s is the actual value of saturation magnetization, A represents the inhomogeneity parameter, B is the magneto-crystalline anisotropy-based parameter, and χ is meant for material susceptibility at a higher value of applied field (H). The value of inhomogeneity constant (A) and additive term ($H.\chi$) may be ignored below Curie temperature (T_c) or in

the presence of higher magnetic field values. The magnetization value of these ferrite samples at a higher magnetic field can be expressed as follows [(Fattouh *et al.* 2021)];

$$M = M_s \left[1 - {}^{B}/_{H^2}\right] \quad (3.14)$$

This relation can be treated as a straight-line equation, where B can be determined as slope, and saturation magnetization (M_s) can be obtained with the intercept on Y-axis in M vs. H^{-2} curve. Other magnetic parameters such as Bohr magneton (N_{BM}), magnetic anisotropy constants (K_1), anisotropy field (H_a), and effective magneto-crystalline anisotropy value (K_{eff}), are calculated using the following relations [(Adeela *et al.* 2016), (Tchouank Tekou Carol *et al.* 2020), (Fattouh *et al.* 2021), (Shekhawat and Roy 2019)]:

$$N_{BM} = \frac{M_w \, X \, M_s}{5585} \quad (3.15)$$

$$K_1 = \left(\frac{\mu_o}{2}\right) M_s . H_c \quad (3.16)$$

$$B = -{}^{H_a^2}/_{15} \quad (3.17)$$

$$K_{eff} = \frac{M_s \sqrt{15.B}}{2} \quad (3.18)$$

Where M_w is the molecular weight of the sample and μ_o is free space permeability ($4\pi \times 10^{-7}$ H/m), M_s is the saturation magnetization value, and H_c is the coercivity field.

3.2.7 Magnetothermal analysis

Magnetothermal analysis has been employed to evaluate the magnetic hyperthermia capability of the ferrite system. The instrument comprises a set of electronic gadgets assembled specifically to determine the time-dependent temperature graph for any ferrofluid. As shown in Fig. 3.7, the resonant controller is attached to the power supply and oscillator to generate a frequency-dependent AC magnetic field within magnetic coils. The resonating current value is used to generate AC magnetic field within helical-shaped magnetic coils. The sample (as a ferrofluid) is placed between these coils to measure the

dynamic temperature using an optical fiber-based temperature sensor. The as-obtained data are displayed and stored in terms of time-dependent temperature graphs [(Mazon *et al.* 2017)].

This heating capability of any ferrofluid is investigated in terms of SAR and ILP values, determined from the time-dependent temperature values in the ferrofluid that is subjected to the alternating magnetic field. The ferrofluid sample placed in a glass vial is mounted inside the solenoid and represents an element of the RLC series circuit. The circuit is supplied by the sinusoidal signal generator with a signal of frequency f [(Skumiel *et al.* 2007)].

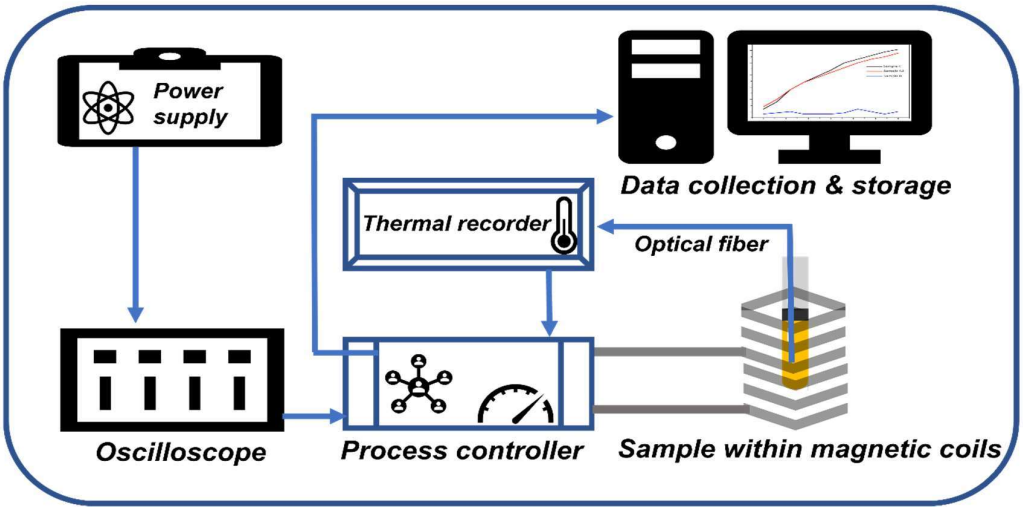

Figure 3.7 Schematic representation of magnetothermal analysis equipment.

In the present work, the magneto-thermal (heating capability) investigations of the stabilized ferrofluids are carried out using the magnetherm instrument (nanoTherics, UK). The SAR values (W/g) of the ferrofluid under the influence of an externally applied AC magnetic field are quantified using the following relationship [(Céspedes *et al.* 2014)]:

$$SAR_{ferrofluid} = C_d \cdot \left({}^{1}/_{M_{np}}\right) \cdot \left({}^{dT}/_{dt}\right) \qquad (3.19)$$

Where C_d represents the specific heat capacity (volumetric) of the dispersant (C_{water} = 4185 J $K^{-1}L^{-1}$), M_{np} is the mass of magnetic nanoparticles present within the unit volume (concentration per ml), (dT/dt) represents the initial heating rate or slope of temperature vs. time graph (measured using linear fitting from 30°C to 35°C). The normalization of SAR values is reported in terms of intrinsic power losses (ILP), which are determined using the following relationship with SAR [(Lanier *et al.* 2019)]:

$$ILP_{ferrofluid} = (SAR).\ \frac{1}{f.H_{AC}^2} \tag{3.20}$$

Where ILP is intrinsic power loss in nHm^2/Kg, H_{AC} is the strength of the applied AC magnetic field at a frequency (f).

3.2.8 Dynamic light scattering analysis

The particle size obtained in a dynamic light scattering (DLS) or photon correlation spectroscopy (PCS) or quasi-elastic light scattering (QLS) instrument is the diameter of the sphere that diffuses at the same speed as the particle being measured. In the present work, the particle size, along with poly-dispersion index (PDI), is measured within a glass cuvette positioned at 4.65 mm from the source, using a dynamic light scattering (DLS) based Zetasizer Nano ZS **(**Malvern Panalytical**)** analyzer. It is a high-performance two-angle particle size, zeta-potential, and molecular size analyzer for the enhanced detection of aggregates and small particles (size may vary within a broad range of 0.3 nm to 10 µm). The system is equipped with a 532 nm 'green' laser source with a narrow band filter (ZEN9052).

Fig. 3.8 suggests that the particle size is analyzed by measuring the degree of incident laser scattering after interacting with the individual particle. The Zetasizer system measures the particle size by determining the Brownian motion of the particles in a sample using DLS and then rendering a size from this using well-known theories. The Brownian motion is explained as the random movement of particles suspended within a liquid phase

due to the bombardment by the surrounding molecules. As the particles are used to move randomly, their moving speed may be utilized to determine the particle size. The particle with a small size moves or diffuses faster than the larger particle. If the particle's position is analyzed with respect to time, the less the movement represents the larger particle size, the more the movement is meant for the smaller particle size [(Raja, P. M. V., & Barron 2021)].

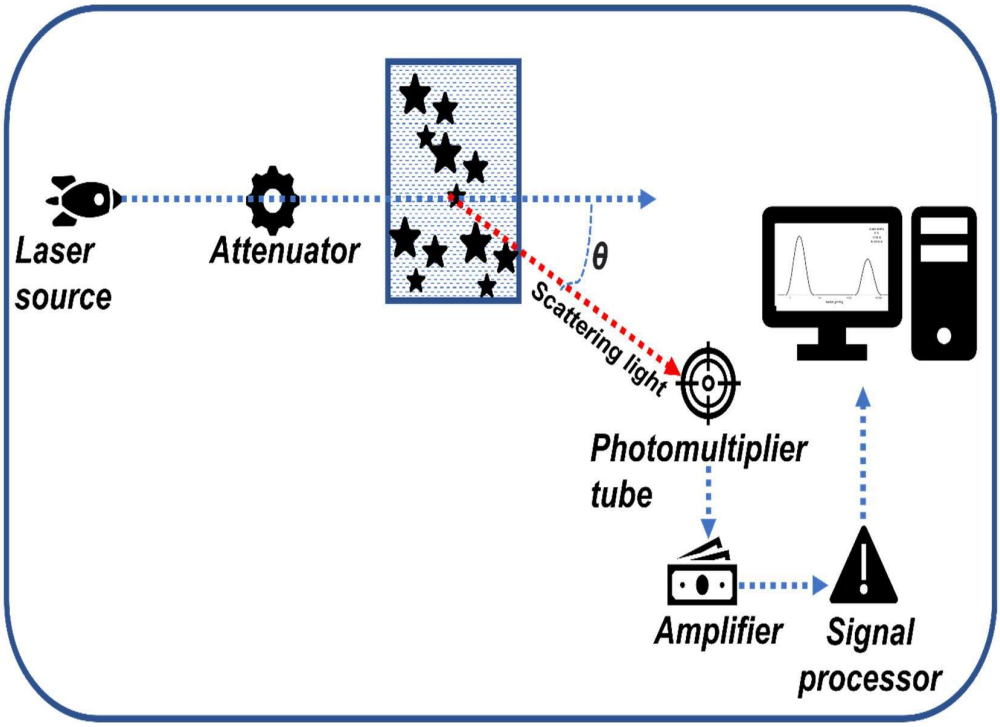

Figure 3.8 Schematic representation of dynamic light scattering-based particle size analyzer.

3.2.9 UV–Vis Spectroscopy

UV-Vis Spectroscopy can be utilized to study its light absorption capability quantitatively by measuring the light intensity that passes through the sample in comparison to reference material or blank, as shown in Fig. 3.9.

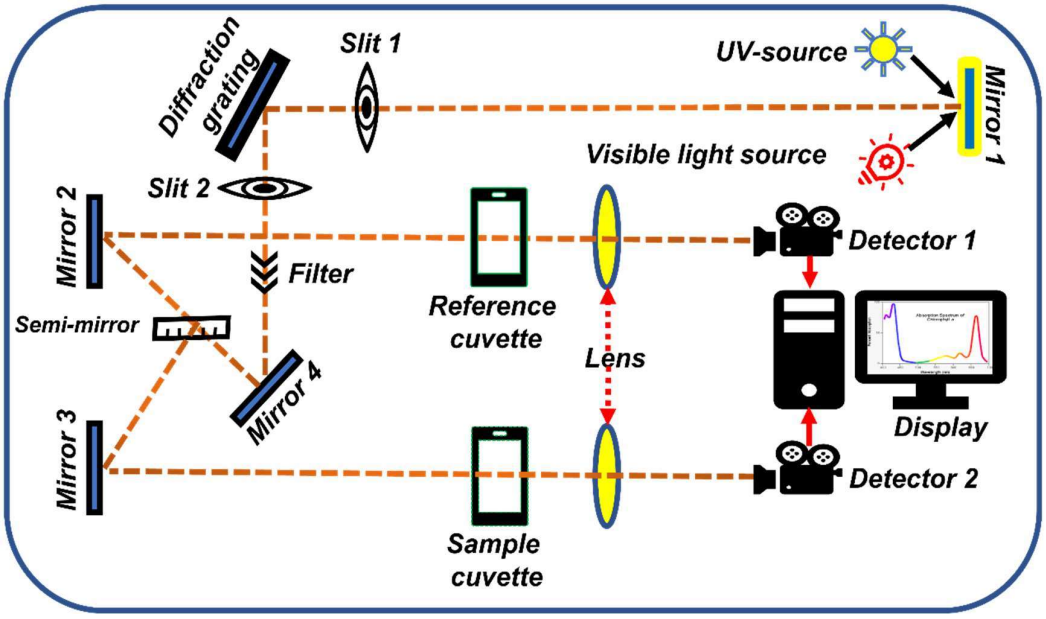

Figure 3.9 Schematic representation of working principle for UV-Visible spectrometer.

The absorbance of light energy or electromagnetic radiation permits the excitation of an electron from its ground state to the first singlet excited state of that material. This characterization technique deals with Beer-Lambert Law, as given below [(Clark 2020)]:

$$E = \log(I_0/I) = \varepsilon_{MA} C_M P_L \quad (3.21)$$

Where E represents the absorbance, I_0 is the initial intensity of light, I is the outgoing intensity through the sample, C_M is the molar concentration of material within the solvent, and P_L is the path length through which the radiation has to interact with the sample (cm), ε_{MA} is the molar absorptivity of that material. In this research work, the UV- visible data is recorded in the wavelength range of 200 to 1400 nm using Agilent Cary 60 UV-Vis spectrometer.

3.2.10 Density measurement

The bulk densities of the sintered pellets (10 mm diameter) samples are measured by the renowned Archimede's principle using deionized water as buoyancy liquid. The

density of a sample has been measured using a weighing balance-based arrangement with an accuracy of 0.0001 g equipped with a density measurement kit (density kit, model no. WDK 200 supplied by Wensar weighing scales ltd.). The pellets are submerged within deionized water for 2 hours to allow the DI water into the pores, facilitated by a vacuum pump arrangement. The bulk density (D_{Bulk}) and percentage porosity ($P_{\%}$) are measured by the following equation [(Berger 2010)]:

$$D_{Bulk} = \frac{W_D}{W_S - W_A} \tag{3.22}$$

$$P_{\%} = \frac{W_S - W_D}{W_S - W_A} * 100 \tag{3.23}$$

Where W_D is the dry weight (taken initially before soaking in water), W_S is the soaked weight, and W_A is the suspended weight of the prepared sample.

3.2.11 X-ray photoelectron spectroscopy

X-ray photoelectron spectroscopy (XPS) is a surface-sensitive analytical technique in which the surface of the material is bombarded using X-rays, and the kinetic energy of the photoelectron emitted from the surface is analyzed. The technique involves two major features, i.e., high sensitivity to surface composition and the ability to reveal the elemental states, which makes it a powerful tool for characterizing various materials. The XPS can be utilized to study all kinds of materials such as semiconductors, plastics, textiles, and metals, except hydrogen and helium. The study of a material's surface becomes quite important while dealing with surface-sensitive phenomena such as adhesion, corrosion, catalysis activity, charge transfer, etc. The working principle of XPS relies on the photoelectric effect, first revealed by Heinrich Hertz in 1887. According to this law, light irradiation causes the emission of electrons from material surfaces. In 1914. the concept of photoemission using X-ray irradiation was first observed by Robinson and Rawlinson. In

contrast, the first application of photoemission as an analysis method was offered by Steinhardt and Serfass in 1951[(Stevie and Donley 2020)].

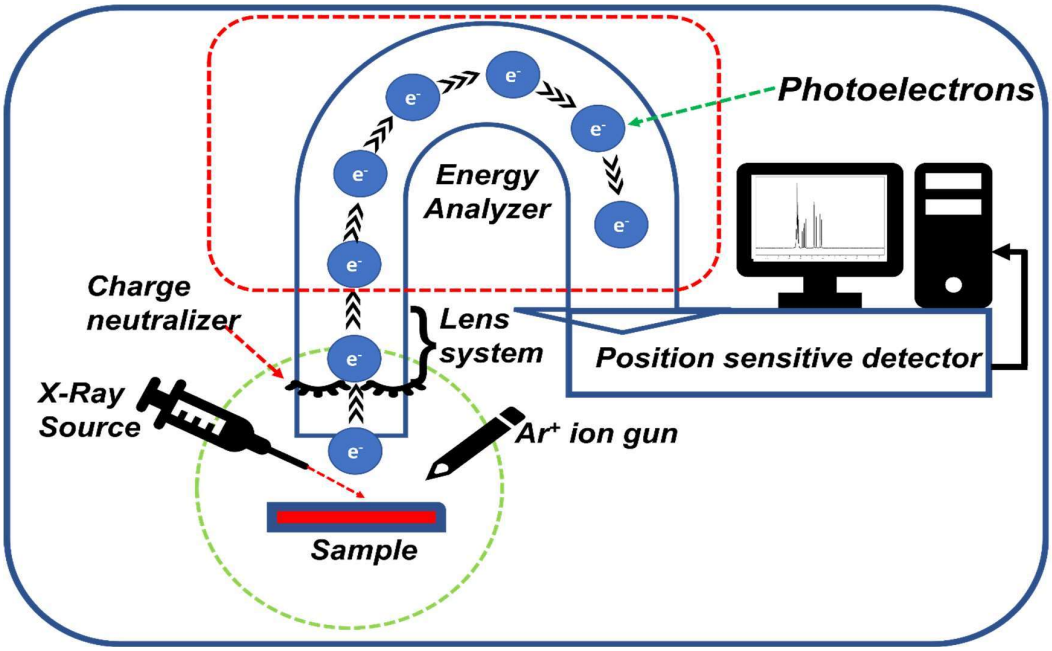

Figure 3.10 Schematic representation of working principle for X-ray photoelectron spectrometer.

In XPS, the sample is irradiated using low-energy X-rays (energy less than ~6 keV). The kinetic energy of the released electrons from the material's surface is analyzed, as shown in Fig. 3.10. The photoelectrons emitted through the surface of the material are generated due to the total energy transfer of incident X-rays to a specific core level electron. This energy transfer phenomenon can be expressed using the following relation [(Good and Horace Facey 2020)]:

$$E_{binding} = E_{photon} - (E_{kinetic} + \Delta) \quad (3.24)$$

Where $E_{binding}$ is the energy of an electron attached to the nucleus, E_{photon} is the energy of the X-ray photons dependent on the X-ray source, $E_{kinetic}$ is the kinetic energy of the emitted electron, Δ is the work function, added as a correction factor for the instrument and

associates the requirement of least energy to release an electron from an atom. For a particular instrument, the value of work function (Δ) and photon energy is known, and the kinetic energy of the emitted electron is determined by the detector. The specific binding energy can be determined from the above relation (Equation 3.24). Based on obtained binding energy, the orbital and subshell (*s*, *p*, *d*, etc.) positions are governed accordingly. By detecting the energy of emitted photoelectrons, XPS allows for the composition and chemical shifts of a material [(Greczynski and Hultman 2020)]. In this research work, the chemical states of elements on the sample surface are investigated using a *K*-alpha X-ray photoelectron spectrometer (XPS) with Al-*K*α micro-focused monochromator (Thermo Fisher Scientific Inc., Waltham, UK). The spectra are recorded in fixed analyzer transmission mode with a spot size of 400 μm at 10^{-8} torr. The as-obtained XPS data is analyzed using Origin Pro 8.5 software to determine the peak positions and their deconvolution.

3.2.12 Vector network analyzer

VNA is an instrument capable of measuring an electrical network's parameters such as gain (dB), insertion phase (degrees), insertion loss (dB), complex transmission components (magnitude and phase), transmission co-efficients (S_{21}, S_{12}), electrical delay (second), electrical length (m), group delay (second), deviation from linear phase (degrees), reflection co-efficients (S_{11}, S_{22}), return loss (dB), impedance, reflection co-efficients vs. time (Fourier Transform), standing wave ratio (SWR) [(Anritsu Company 2013)]. The elementary function of a network analyzer is to analyze the reflected & incident waves (both phase & amplitude) at the diverse ports of the Device Under Test (DUT). This VNA consists of both a source (to produce a known stimulus signal) & set of receivers (to adopt variations in stimulus signal caused by the DUT).

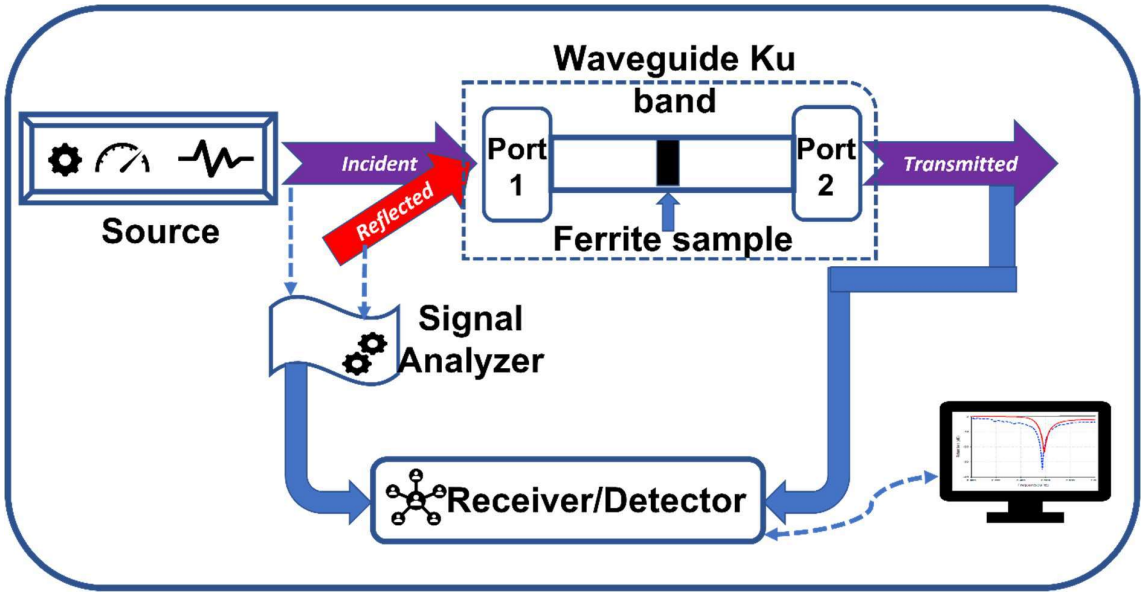

Figure 3.11 Block diagram of working principle for vector network analyzer.

VNA measures three different types of measurement based on transmission, reflection, and scattering of waves. The scattering parameter-based measurements include the determination of s-parameters like S_{11}, S_{12}, S_{21} & S_{22}. The block diagram of VNA (Fig. 3.11) includes four important components, i.e., signal generator (sweep oscillator or synthesized signal generator to provide the incident signal which stimulates the DUT), signal separator (mainly power splitters or high impedance probes or bridges or directional couplers utilized to split different signals like incident, reflected & transmitted), receiver or detector (broadband tuned receiver or diode-based broadband detector), and controller/processor or display (produces the results as favored by the operator by intermediating frequency signal & displays the information on the screen) [(National Instruments 2012)].

The operational working of VNA includes the generation of signal through source, which incident over the DUT. Subsequently, the signal separator device splits incident, reflected & transmitted signals. The receiver or detector converts the frequency level from

microwave frequency to lower frequency to provide easy processing. Finally, the processor or display processes these signals & displays them in the desired format on the screen. In this research work, the variation within the electrical permeability, permittivity, and S parameters are examined using the waveguide method through the vector network analyzer (VNA) (Keysight Tech, E5071C).

3.2.13 Fluorescence microscopy

Fluorescence is a physical effect instigated during the emission of light energy due to irradiation of any substance with light or further forms of electromagnetic radiation. The optical microscope, which utilizes fluorescence and phosphorescence along with reflection and absorption to investigate the optical properties of organic and inorganic matters, is termed fluorescence microscopy (discovered by August Kohler, Carl Reichert, and Heinrich Lehmann). It helps to visualize an entity's sub-cellular and interior structures with improved precision. The emission of light occurs within nanoseconds after the absorption of light (having a shorter wavelength). The stokes shift (variance between the stimulating and released wavelengths) makes fluorescence microscopy a powerful tool. It became significant to see the selective part of matter, which provides fluorescent signals by blocking the exciting light totally. To enhance the contrast within fluorescent micrographs, the objects need to be stained with light-absorbing agents [(Lichtman and Conchello 2005)].

The sample must be stained with any fluorescent dye or fluorophore (in the present work, Hoechst and Alexa FlourPhalloidin dyes are used) before observing with fluorescence microscopy. The incident light (UV rays or blue light having higher energy and short wavelength) produced by a light source (mercury vapor arc lamp) is allowed to pass through an excitation filter where all other non-specific wavelengths of light are

removed. This filtered light ray is used to irradiate the sample after reflecting from a dichroic filter. The fluorochrome available over the sample surface absorbs the incident wavelength (with high energy) and releases the shorter wavelength (less energy). This emitted light wave is detected by the detector after being filtered through a specific wavelength-based emission filter and displayed in the form of a glowing image format with a dark background. In this research work, the fluorescent images of the stained cells (nuclei and cytoskeleton) are observed using a fluorescence microscope (LV100 ND, Nikon).

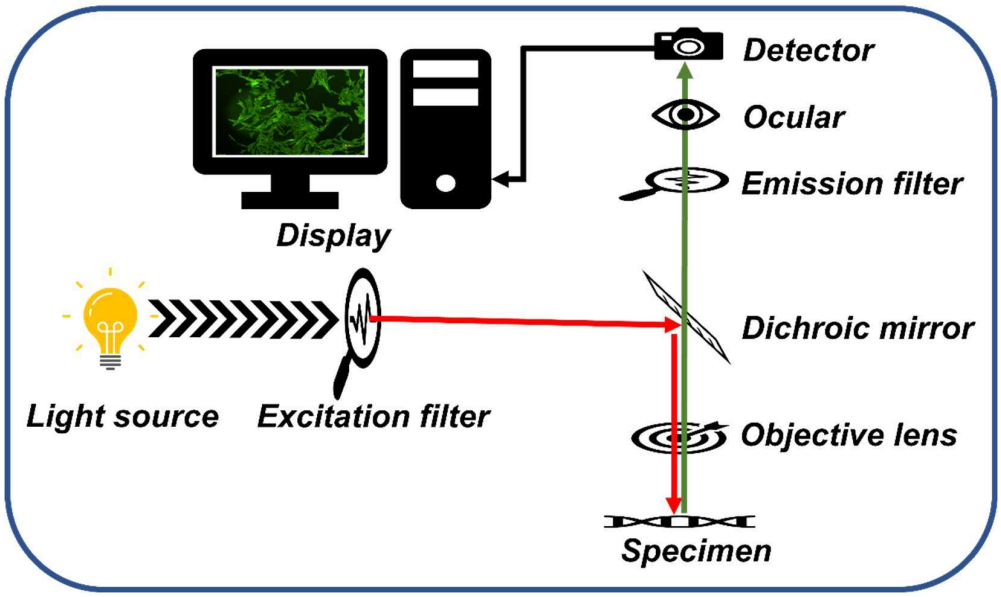

Figure 3.12 Schematic representation of working principle for fluorescence microscopy.